UCRL-CR-121294 Rev 1

Optimization of X-ray Sources for Proximity Lithography Produced by a High Average Power Nd:Glass Laser

P. Celliers, L. B. DaSilva, C. B. Dane, S. Mrowka, M. Norton,
J. Harder, L. Hackel and D. Matthews
University of California, Lawrence Livermore National Laboratory
Livermore, CA 94550

H. Fiedorowicz and A. Bartnik
Military University of Technology, Insititue of Opteoelectronics, Laser Plasma Interaction Section, 01-489 Warsaw 49, Poland

J. R. Maldonado
IBM microelectronics, Rt. 52, Hopewell Junction, NY 12533

J. A. Abate
600 Mountain Ave., AT&T Bell Labs, Murray Hill, NJ 07974

This paper was prepared for submittal to U.S. Department of Defense
Advanced Research Projects Agency
Arlington, VA

July 1995

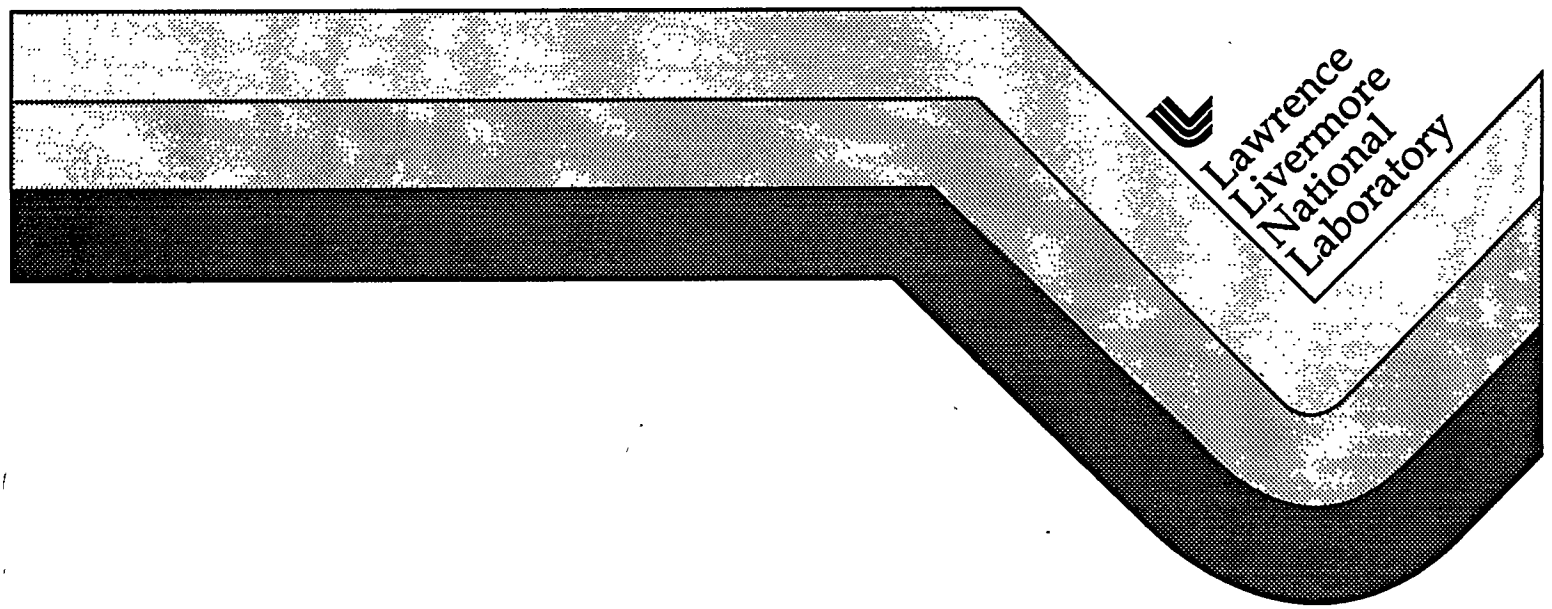

Disclaimer

Optimization of x-ray sources for proximity lithography produced by a high average power Nd:glass laser*

P. Celliers, L. B. DaSilva, C. B. Dane, S. Mrowka, M. Norton, J. Harder, L. Hackel and D. L. Matthews
University of California, Lawrence Livermore National Laboratory, Livermore, California, 94550

H. Fiedorowicz and A. Bartnik
Military University of Technology, Institute of Optoelectronics, Laser Plasma Interaction Section, 01-489 Warsaw 49, Poland

J. R. Maldonado
IBM Microelectronics, Rte 52, Hopewell Junction, New York, 12533

J. A. Abate
600 Mountain Ave., AT&T Bell Labs. Murray Hill, New Jersey, 07974

Abstract

We measured the conversion efficiency of laser pulse energy into keV x-rays from a variety of solid planar targets and a Xe gas puff target irradiated using a high average power Nd:glass slab laser capable of delivering 13 ns FWHM pulses at up to 20 J at 1.053 μm and 12 J at 0.53 μm. Targets where chosen to optimize emission in the 10 - 15 Å wavelength band, including L-shell emission from materials with atomic numbers in the range Z=24-30 and M-shell emission from Xe (Z=54). With 1.053 μm a maximum conversion of 11% into 2π sr was measured from solid Xe targets. At 0.527 μm efficiencies of 12-18%/(2π sr) were measured for all of the solid targets in the same wavelength band. The x-ray conversion efficiency from the Xe gas puff target was considerably lower, at about 3%/(2π sr) when irradiated with 1.053 μm.

*** Research performed for the US Department of Defense Advanced Research Projects Agency.**

I. INTRODUCTION

The concept of a laser-based proximity lithography system has advanced to the point that a detailed design of a prototype system capable of exposing 40 wafer levels per hour at 0.12 μm feature size appears to be technically feasible with high average power laser technology. Various technological choices need to be made regarding the specific laser driver technology to be used and specific target material and design. The research described in this article focused on measuring and optimizing the x-ray yields produced with one particular choice of laser driver intended for x-ray production in a proximity lithography system.

X-ray yields from laser-produced plasmas have been investigated in great detail for nearly two decades, and have been examined over a wide variety of laser parameters (wavelength, pulse duration, focused intensity) as well as target material and x-ray emission wavelengths.[1-10] A number of studies have focused specifically on lithography applications to match target materials with realistic laser parameters in order to produce the required x-ray spectrum (keV x-rays) at an acceptable yield.[11-17] X-rays from laser-produced plasmas in the 1 keV energy range required for proximity lithography are produced most efficiently with focused laser intensities around 10^{13} W/cm^2 and from targets with atomic number in the range Z= 26-30 (Ne-like ions, L-shell emission) or Z=53-56 (Ni-like ions, M-shell emission). As a general finding, x-ray yields are known to improve substantially with decreasing laser wavelength.[2, 3, 5] X-ray yields from laser-produced plasmas also depend on the pulse duration which determines the characteristic plasma volume achieved during the pulse. High conversion efficiency (better than 10%/2π sr) has been usually observed with moderate duration pulses (0.5 - 10 ns).[9, 14]

However, high conversion efficiency can also be achieved with shorter pulses (< 100 ps) in combination with a weak prepulse to generate a long scalelength plasma.[10, 18] For pulses longer than 10 ns it is not clear, from the findings of previous studies, whether high conversion efficiency can be achieved. Early experiments with 8 ns Nd:glass laser pulses indicated that efficiencies around $8\%/2\pi$ sr could be achieved;[1] however, experiments with 30 ns KrF pulses focused to more than 10^{14} W/cm^2 failed to achieve yields comparable to measurements with shorter pulses at the same wavelength.[15] A practical limit on the pulse duration of less than about 5 ns was suggested by Chaker *et al.*[17], although this conclusion was tentative in the absence of experimental data. The requirements of high average power with high focused intensities and moderate pulse duration are potentially in conflict with the pulse parameters of current high average power laser technology, which operate more reliably with rather long pulse durations in the range of 10 - 15 ns duration for Nd:glass technology and 25 - 30 ns for excimer lasers.

One potential laser driver for proximity lithography is a high average power Nd:glass slab design operating with high pulse energy and moderate repetition rate. Currently the most advanced realization of this technology is available at Lawrence Livermore National Laboratory,[19] and consists of a flashlamp pumped system capable of producing near diffraction-limited pulses with approximately 13 ns FWHM duration at energies of around 20 J at a rate of 6 Hz to produce an average power of 120 W. The design is scaleable to higher average power by increasing the pulse energy and/or repetition rate; average powers approaching 2 kW are envisioned. An important characteristic of this high average power capability is the utilization of phase conjugate wavefront correction[20] to ensure a uniform intensity and a near

ideal phase front in the final pass of the slab amplifier, which is necessary to ensure reliable operation. This technology operates most effectively with a rather long pulse duration of 12 - 14 ns, which raises the issue of whether the x-ray yields produced with this laser can approach the maximum yields observed with shorter pulses. This question was examined experimentally in the work described in this report.

In this study we measured and optimized the x-ray conversion from several L-shell emitters (Fe, Cu, Zn, brass, stainless steel), and one M-shell emitter (Xe). The studies with Xe included measurements from a cryogenic solid target as well as a preliminary investigation of a gas puff target. Both forms of the Xe target offer the potential to design a source with considerably reduced debris generation. All targets were investigated at two operating wavelengths of the laser: the fundamental wavelength 1.053 μm; and the second harmonic, 0.527 μm.

II. EXPERIMENT

The experiments utilized several diagnostics and target configurations, which we describe in detail in this section. We measured absolute x-ray yields using a set of absolutely calibrated and filtered photoconductive diamond (PCD) detectors. We also measured the x-ray spectrum for each target type and for all variations of other input parameters, such as laser pulse energy, wavelength and focusing conditions; the detailed emission spectra were found to vary with all of these parameters. We used the measured spectra in the analysis of the data produced by the PCD detectors. This was essential to obtain accurate measurements since the x-ray fluence striking each PCD

detector depended on both the filter transmission function and the detailed emission spectrum of the source.

II (a) Laser parameters

For the experiments with solid planar targets the experimental layout is shown in Figure 1. The laser was focused through a 330 mm lens into the center of the experimental chamber onto a planar target oriented at 45° to the laser axis. Laser energy was monitored with a fast pyroelectric detector, and cross-calibrated with a calorimetric energy meter. Pulse energy was variable from about 1 - 20 J at 1.053 μm, and 0.5 - 12 J at 0.527 μm wavelength. The beam delivered to the target chamber was square in cross-section measuring 25 mm on each side, and produced an f/13 focus with the 330 mm focal length lens we used. The beam focus was adjusted by translating the lens. In a separate test of the beam quality the far field pattern of the 0.527 μm beam focused with the 330 mm lens was imaged onto a CCD camera using a well-corrected microscope objective. At best focus we found that 80% of the beam energy was contained within a diameter of 27 μm, equivalent to about 1.5 x the diffraction limit. The maximum focused intensities achieved with this beam quality reach as high as 7×10^{13} W/cm^2 for 1.053 μm and 2×10^{14} W/cm^2 for 0.527 μm light. These peak intensities meet or exceed the intensities required to obtain high x-ray yields in the keV range.

II (b) Solid targets

The target mount consisted of an x-y-z translation stage with an aluminum mounting frame for attaching the target. Motion in a plane parallel to the target surface (x-y) allowed us to position a fresh surface of the

target in the beam for each shot while maintaining the same axial position relative to the laser focus. All of the solid targets were available in the form of tapes or thin plates which could be mounted directly on the frame. For most of these materials the target thickness was much larger than typical ablation depths. However in the particular case of Fe the target consisted of a thin layer of 3-5 μm of Fe powder bonded to a mylar tape substrate. This "mass limited" target is designed to provide enough material to produce x-rays while limiting debris production.

In the particular case of solid Xe the target apparatus consisted of a 1 mm thick copper plate connected to a cold finger with a length of copper braid, and cooled to approximately 20 K. A solid Xe layer was formed by condensing Xe gas onto the cryogenic surface to produce a thin (approximately 100 μm thick) layer on the copper substrate. Although the melting point of Xe (at atmospheric pressure) is around 160 K, a temperature of 20 K was required in vacuum in order to maintain a low enough Xe vapor pressure to produce a stable condensed layer on the copper substrate and to minimize reabsorption of the Xe x-ray emission by residual cold Xe gas in the chamber.

II (c) Gas puff target

The gas puff valve used to examine yields from Xe gas has been described in previous work.[21] It was supplied with a reservoir of Xe maintained at 10 atm, and produced gas pulses lasting for several hundred μs duration from nozzle apertures varying from 500 μm to 1000 μm in diameter. The nozzle from the gas puff valve was oriented coaxial relative to the laser beam with the beam directed straight into the nozzle (Figure 2). X-ray yield was monitored with a PCD array placed to view the plasma from an orientation

perpendicular to the laser axis and situated at the nozzle exit. The x-ray spectrometer and the pinhole camera also viewed plasma from a perpendicular orientation to the axis and at different azimuthal positions.

II (d) Curved crystal spectrograph

A curved potassium acid phthalate (KAP) crystal spectrograph recorded x-ray spectra from a direction of 90° relative to the laser axis and 45° to the target normal. The spectrometer consisted of three separate KAP crystals each bent to a radius of 79 mm, situated about 350 mm from the plasma. A high resolution CCD camera system operating with 16-bit readout resolution[22] was used to record the spectra. The detector consisted of a backilluminated Tektronix TK1024 CCD chip. The system was sensitive enough so that all spectra recorded in these experiments were produced with a single laser pulse. To obtain the complete spectrum the KAP crystals were placed at slightly different standoff distances from the plasma to sample the 9 - 19 Å spectral region in overlapping segments. To block out visible and UV portions of the spectrum one or two layers of a light tight aluminized mylar film (5000 Å Al/1.5 μm mylar) was placed at the entrance to the spectrograph. This film was subject to occasional damage from target debris, and was checked and replaced at appropriate intervals.

We performed wavelength calibration of the spectrometer by identifying known features of the Fe and Cu L-shell spectrum and applying a low order polynomial mapping from detector position to a wavelength scale. Within the 9-19 Å band the CCD array detector responds linearly to the x-ray fluence independent of wavelength. We corrected the raw data to account for the filter transmission and the KAP crystal reflectivity. The aluminized mylar

transmission was independently calibrated at an in-house facility to determine its transmission over the 9-19 Å wavelength band. The KAP reflectivity has been previously calibrated by Henke *et al.* [23]

II (e) Absolutely calibrated PCD and yield measurements

X-ray yields were recorded with a set of 4 filtered type IIA photoconductive diamond (PCD) detectors.[24] These were mounted in a compact 2 x 2 square array situated 15.9 cm from the target at an angle approximately normal to the target surface. For all measurements the PCDs were biased with 600 V, and the signal was coupled through a capacitor into a 50 ohm cable connected to a high speed digital oscilloscope for recording. These detectors have been used in a number of previous x-ray yield experiments at LLNL,[25] and have been absolutely calibrated.[26] Within the 9-19 Å wavelength band observed in these measurements they have a flat wavelength response. For the bias conditions and spectral range used in the measurements reported in this work the sensitivity of these devices was nominally 7.5×10^{-4} A/W. An uncertainty of approximately 20% on this value as reported in the original absolute calibration was assumed.

Examples of a PCD signal trace and a trace of the laser pulse recorded on high speed oscilloscopes are shown in Figure 3. The x-ray pulses displayed the same temporal structure, if any, that was produced in the laser pulses. The FWHM pulse duration of the x-ray signals observed from solid targets was similar to but somewhat shorter than the laser pulse by an amount of approximately 20% - 30%. Hence the x-ray pulses from solids were typically 10 ns FWHM, while the laser pulse was 12 - 14 ns FWHM.

We monitored contributions from various parts of the x-ray spectrum using a set of four different filters on the PCD detector array. The filter materials, thicknesses and transmissions are displayed in Figure 4. The filter foils were mounted on 9 mm diameter washers with 5 mm diameter apertures to allow easy manipulation and placement in the detector housing. All of these foils were manufactured commercially by vacuum evaporation;[27] furthermore, all foils of each type originated from the same batch in the fabrication process. Several samples from each filter type were separately calibrated at a facility at LLNL to determine an accurate thickness. Prior to all measurements we performed a cross-calibration of the individual PCD sensitivities. To do this we placed nominally identical 2 μm Zn filters on all detectors and recorded signals from a Fe or type 302 stainless steel laser-produced plasma. Several data points were taken for each of 3 rearrangements of the individual filters in the filter set so that we could eliminate effects due to variability in the filter transmission. We found a variation in detector sensitivity among the four devices used in this work amounting to a ±20% spread. The extracted filter transmissions were also consistent with a 10 - 15% variability from one piece to the next. Based on these uncertainties alone, the absolute uncertainty in yield for these measurements is around ±25%. However, relative uncertainties (comparison of different target materials or laser parameters) were around 10%, which was determined primarily by shot-to-shot variations.

To determine the absolute x-ray yield, we integrated the recorded oscilloscope signals to produce a value proportional to the total x-ray fluence striking the detector. We then converted this raw data to an absolute measure of the x-ray fluence by factoring in corrections to account for detector

sensitivity, solid angle, filter transmission and the emission spectrum. Simultaneous measurement of the spectrum is crucial for an accurate determination of the fractional weight of the spectrum viewed by each channel. We determined x-ray yields by weighting each detector signal by a factor inversely proportional to the known filter response multiplied by the measured spectrum at each incident energy. We then obtained the resulting conversion efficiency from an average of the contributions measured from each channel, and the known input laser energy.

The CCD detector on the spectrometer also provided an accurate method of assessing relative x-ray yields (from one target to the next, or for changes in other parameters, such as laser energy). This provided us with a cross-check against the yields inferred on the basis of the PCD measurements. We found good agreement between the relative yields determined from integrating the spectrum recorded on the CCD, and the signals measured with the PCD array.

II (f) Pinhole camera

We monitored plasma source size with an x-ray pinhole camera coupled to a video CCD and a computer-controlled readout. The pinhole was placed about 3 cm from the target and operated at a magnification of 2-3. The x-ray spectrum was filtered with 18 μm Al foil hence was sensitive mostly to the 8 - 12 Å portion of the emitted spectrum.

III. METHODS

III (a) Planar solid target optimization

For each target type and laser wavelength investigated (except the gas puff source) the x-ray yield was optimized and measured with a standard procedure consisting of two parts. Firstly, we conducted a focal scan consisting of a series of shots examining yield as a function of axial lens position at maximum laser energy (20 J at 1.053 μm and 12 J at 0.527 μm). The lens position corresponding to maximum yield as determined from the PCD measurements was identified from this procedure. Secondly, we fixed the lens at its optimum position and measured x-ray yield while the laser energy was varied throughout the available range below the maximum setting. Laser energy was easily adjusted by rotating a waveplate within the pre-amplifier chain to control the pulse energy prior to the final amplifier passes. Both the temporal pulse shape and spatial beam parameters (focus position) were unaffected by this adjustment.

An example of the variation of x-ray yield with lens position is displayed in Figure 5, for Cu and type 302 stainless steel irradiated with 1.053 μm laser light. We found in general that the x-ray yield reached a broad maximum within a ±1 mm range of the lens focus. The position of optimum conversion was largely independent of the target material, varying by an amount of approximately ±0.5 mm for different materials.

Pinhole photographs of the x-ray source region throughout the focal scans for both 1.053 μm and 0.527 μm are shown in Figures 6 and 7 respectively. The double lobed structure apparent at lens positions of 14 and 15 mm in Figure 6 originates from the intensity distribution in the square beam as it

approaches the focus. Similar lobed structures evident in the 0.527 μm scan also originate from laser intensity modulations near best focus, although the pattern is less regular. Also plotted in Figures 6 (b) and 7 (b) is the variation of x-ray source size measured in these focal scans. The emitting region of the plasma is considerably larger than the beam diameter close to best focus since under no conditions did we observe an x-ray source region smaller than about 150 μm in diameter, a value which is 3–5 times larger than the beam diameter expected at best focus for the 1.5 x diffraction limited beam. To analyze these images we assumed that the size of the x-ray emitting region correlated with the spatial extent of the laser intensity distribution illuminating the plasma. We took the point where the observed source diameter reached a minimum to be the lens position corresponding to best focus. Using this to identify the focus we also display the geometrical extent of the focal cone for the f/13 focus in these figures for comparison with the data. It is evident that the emitting plasma region is larger than the beam diameter throughout most of the range of lens positions where significant x-ray emission was observed.

The most important information from these sequences is an assessment of the size of the x-ray emitting region in the source, and an approximate idea of the laser intensity illuminating the plasma at these optimum positions. At the lens position corresponding to the optimum x-ray yield the diameter of the source region evident in these sequences is around 280 μm for 1.053 μm laser light and 240 μm for 0.527 μm light. It is also evident that the lens position corresponding to best yield does not correspond to the position of best focus, although it is much closer to best focus for 0.527 μm light than for 1.053 μm light. (X-ray yield on the converging side of the 1.053 μm focused

beam should be similar to the diverging side; for all measurements reported here the beam was focused on target with a diverging focus.) Average beam intensities illuminating the plasma at these lens positions can be estimated from the geometrical extent of the focal cone and the distance of the optimum lens position from best focus. For 1.053 μm the beam size at optimum focus was ~190 μm diameter, to produce a beam intensity ~5 x 10^{12} W/cm^2. For 0.527 μm light the beam diameter was approximately 100 μm, a factor of two smaller than for the optimum 1.053 μm situation, producing intensities ~1.2 x 10^{13} W/cm^2.

III (b) Angular distribution

For planar targets we also measured the angular distribution of x-ray yield. All yield measurements with the PCD array, described above, were recorded at target normal where the yield is expected to reach a maximum. To ease comparison with other reported work, we report the x-ray yield in this work as the conversion fraction into 2π sr as if the angular distribution were isotropic and equal to the angular fluence measured at target normal. The angular fluence varies relative to target normal, and depends on target material, laser wavelength, laser pulse duration and other factors. Generally the yield is reduced away from target normal and can be fitted with a $\cos^{\alpha}\theta$ distribution, where $\alpha \leq 1$, and the total conversion into 2π sr is less than the fraction reported in this work. There may be reasons to place the lithography exposure system at a location other than target normal, for example, to mitigate against debris, which is also maximized at target normal. Thus an assessment of the angular distribution is important to ascertain any reduction in x-ray yield at other angles.

We carried out the angular distribution measurements using Fe or type 302 stainless steel targets at the optimized conditions for both wavelengths. We fitted all PCD detectors with 2 μm Zn filters which transmit the main component of the Fe spectrum. The detectors were arranged in four angular positions in the plane of the laser beam spanning angles from 18° to 75° from the target normal. For each measurement we took several sets of shots. Between each set we rotated the Zn filters through the detectors, in order to eliminate effects due to variations in the filter transmissivities. Results from these measurements, displayed in Figure 8, will be discussed below.

III (c) Xe gas puff

Optimization of the gas puff target followed a different procedure than for the planar solid targets. To optimize the x-ray yield from the gas puff we varied the position of the laser focus and the relative timing between the valve opening and the laser pulse. Following a set of empirical studies where these two parameters were systematically adjusted we found that the timing was the most important parameter. The gas pulse produced from the valve lasted for a duration of approximately 1 ms. The variation of x-ray yield with delay is caused by the variation in gas density emerging from the nozzle, which reached a broad maximum during the gas pulse. We expect x-ray yields to increase with increasing atomic density. No measurements as a function of gas pressure were attempted since the particular valve system used was operating at its maximum pressure limit of approximately 10 atm.

IV. RESULTS

IV (a) Planar solid targets

X-ray yields from all of the solid targets are summarized in Figure 9 where the optimized yield for each material at both wavelengths is compared. High x-ray yields using the longer wavelength emitters (~14 Å) were obtained with 1.053 μm laser drive wavelength, with the best examples of these being type 302 stainless steel and solid Xe. Conversion efficiency of these targets was approximately 10%/2π sr at the target normal. Conversion efficiency for shorter wavelength emitters using 1.053 μm was significantly less, dropping to less than 4%/2π sr for Zn targets emitting around 10.5 Å. we observed a significant improvement in x-ray yield with 0.527 μm light, where conversion efficiencies for all targets were around 12%/2π sr or better. For the range of shorter wavelength emitters including Cu, brass and Zn this represents a factor of 3 - 4 improvement in the conversion efficiency measured at target normal. Since the energy conversion efficiency for doubling the laser light frequency is expected to be around 80%[19], this result indicates that operation at 0.527 μm will provide a substantial improvement in conversion of energy from the fundamental laser wavelength to x-rays in the 10 - 12 Å band, using a frequency-doubled laser.

It is interesting to note that the conversion efficiency measured with 302 stainless steel was the highest of all the materials tested, and is significantly higher than for the pure Fe tape. This improvement is apparent at 1.053 μm light, and becomes quite dramatic with 0.527 μm light, where the optimum conversion exceeds 16% for type 302 stainless steel.

X-ray spectra

A catalogue of spectra for all of the materials tested, and at both laser wavelengths is displayed in Figures 10 and 11. Also identified on the spectra are integral curves depicting the integrated conversion fraction through the range of emission wavelengths extending from short to long wavelengths. With 1.053 μm laser irradiation the L-shell emitters including Cu, Zn, Fe, brass and stainless steel targets all display the characteristic Ne-like spectra (Figure 10) with the 2p - 3s, 2s - 3p, and 2p - 3d emission lines all prominently visible. The Fe and stainless steel targets also displayed spectral features characteristic of F-like and O-like ionization stages. With 0.527 μm irradiation the F-like and O-like emission is also evident in the Cu brass and Zn spectra (Figure 11). The additional emission from the higher ionization stages tends to shift the spectra towards shorter wavelengths.

All of the Xe spectra display distinct wavelength bands with a main component emitting at wavelengths from 10 - 15 Å, and second component in the 17 - 20 Å. The prominent features in the Xe spectra in the 12 - 14 Å range originate from transitions in Ni-like and higher ionization stages. These features, especially evident in Figure 11 (c), include several unresolved transition arrays that can be identified[28] to originate from 3d - 4f transitions in Ni-like (14.3 Å), Co-like (13.7 Å), Fe-like (13.3 Å), Mn-like (12.8 Å) and Cr-like (12.4 Å) ionization stages. The emission in the 10 - 12 Å range originates from 3d - 5p,5f and 3d - 6p,6f transitions in these ionization stages. The longer wavelength emission in the 17 - 20 Å band originates from 3d - 4p transitions. This part of the spectrum, comprising about 20 - 30% of the emitted energy, was also included in our conversion measurements; although this component is of little utility for lithography applications. The longer

wavelength 3d - 4s transitions were not observed in this work because they are situated around 21 Å, beyond the range of the measurement. Excluding the longer wavelength component (i.e. excluding wavelengths > 16 Å) the Xe conversion measured with 1.053 light is less than 10%/2π sr, but still comparable to the type 302 stainless steel conversion. With 0.527 μm light the Xe spectrum becomes harder, shifting to shorter wavelengths, and the total conversion improves to around 12%/2π sr.

The improvement in yield obtained with type 302 stainless steel as compared with pure Fe targets is encouraging and supports the idea that x-ray yield can be improved by mixing several elements of similar atomic number to fill out the emission spectrum. This is demonstrated most clearly in Figure 11 (a) which shows the dense spectrum of stainless steel as compared with the pure Fe spectrum displayed in Figure 11 (b). Stainless steel is an alloy comprised mainly of several transition metals with atomic numbers from Z = 24 through Z = 28 (the chemical composition of type 302 is approximately: Fe, 70%; Cr, 18%; Ni, 9%; and Mn, 2%). The increased yield from the alloy occurs because the strongly emitting lines characteristic of each element are optically thick, or nearly so in the high density plasmas produced with solid targets; thus, the reduced concentration of Fe found in the stainless steel plasma as compared with that produced from pure Fe targets does not lead to a noticeable reduction in the intensity of the characteristic Fe spectral components, while the other alloyed elements in stainless steel provide emission features that fill in the gaps in the spectrum.

Pulse energy dependence

An important characteristic of all of the conversion measurements from planar targets reported in this work is an increasing x-ray yield with pulse energy. For all materials we observed the conversion efficiency to increase monotonically from near zero at low pulse energies, and increase to a saturation value before leveling off. Within the energy range available there was no evidence of a regime where conversion fraction decreased with increasing pulse energy. The saturation value varied with the target material and the laser wavelength. Examples of the energy dependence of the conversion and the saturation behavior for Cu and type 302 stainless steel are shown in Figures 12 (a) and (b). The saturation level for efficient conversion with type 302 stainless steel (median emission wavelength at 15 Å) is evidently lower than for Cu (median emission wavelength at 11.5 Å); saturation appears to be reached around 5 - 10 J for type 302 stainless steel. In the case of Cu it is not clear that the dependence of x-ray conversion efficiency with energy reached a final saturation level at the maximum laser pulse energies available in these experiments. Correlated with the dependence of conversion efficiency on pulse energy was a clear shift in the x-ray spectrum for any given target to shorter wavelengths with increasing pulse energy. This is expected from the fact that increasing pulse energies produce higher intensities and drive hotter plasmas.

These pulse energy dependences are most easily understood in light of previous 0.5 ns pulse duration work by Chaker *et al.*[14], in which conversion into keV x-rays from Cu targets was observed to drop abruptly below intensities of around 5×10^{12} W/cm^2 for 1.06 μm laser light. Optimum conversion efficiencies for Cu measured in this work are comparable to the

values reported by Chaker *et al.* As noted above our procedure for optimizing the conversion by scanning the focus automatically places the irradiance near this saturation intensity and not necessarily at the best focus. Consequently the measurements at decreasing pulse energy will produce lower than optimum intensities, and therefore produce lower x-ray yields. An implication of this interpretation is that it may be possible to attain high yields at lower pulse energies using a faster focusing lens (say f/4 instead of f/13), which will produce the needed intensity. However, we stress that achieving 10^{13} W/cm^2 is necessary but may not be sufficient to achieve high yields (with long pulses)–this possibility needs to be explored experimentally. In our research, no attempts were made to exploit this method of obtaining high conversion efficiency at lower pulse energies.

Laser drive wavelength dependence

As a general rule the conversion fraction (laser energy to x-ray energy) into 2π sr is higher with 0.527 μm laser light as compared with 1.053 μm laser light. The effect is most accentuated for the short wavelength (10 - 12 Å) emitters (Cu, Zn, and brass) where the conversion fraction improves by a factor of 3 - 4 times over the 1.053 μm result. This dramatic improvement in conversion for the shorter wavelength emitters using frequency doubled laser light more than compensates for losses introduced by converting the fundamental to the second harmonic, and provides a means to obtain high x-ray yields at a range of desired wavelengths spanning 10.5 Å (Zn) through 15 Å (302 stainless steel) with a single laser driver.

Similar to spectral shifts that we observed with increasing pulse energy, we also observed a clear shift of the spectra of the various target types to

shorter wavelengths when the drive wavelength was changed from 1.053 μm to 0.527 μm. This spectral dependence is consistent with the improved coupling of the laser light into plasma heating at higher densities, and with the improved conversion.

Angular distribution

The angular distributions measured for both drive wavelengths irradiating Fe or type 302 stainless steel targets are displayed in Figure 8. Fits to a $\cos^{\alpha}\theta$ distribution yielded $\alpha \sim 0.2$ for 1.053 μm irradiation and $\alpha \sim 0.6$ for 0.53 μm irradiation. Neither of these angular distributions are Lambertian ($\alpha = 1$). In the case of 1.053 μm the emission is very close to being isotropic, such that at angles of 60° to 70° from the target normal the observed yield remains at 80% or more of the peak yield at target normal. At 0.53 μm the emission is closer to Lambertian, with the yield reduced to 1/2 of the peak at angles > 65° off target normal. The difference in angular distribution reflects the difference in laser light coupling between the two wavelengths. The shorter wavelength couples much more efficiently into higher density plasma layers which are optically thick and situated closer to the target plane, thus producing a physical situation closer to that of a planar optically thick Lambertian surface emitter.

IV (b) Xe gas puff

We observed much lower x-ray yields from the Xe gas puff than from the solid Xe targets. The best conversion fraction we obtained with 1.053 μm irradiation, was around 3% into 2π sr; with 0.527 μm light the conversion was substantially poorer, around 0.5%/(2π sr). The x-ray spectra observed from

the 1.053 μm irradiated gas puff display similar features as the solid Xe targets irradiated at 1.053 μm, indicating that the gas puff plasma reaches similar temperatures and ionization states. The poorer conversions obtained with the gas targets originates from the fact that these targets are at much lower densities than solids, such that the laser energy is not efficiently coupled into the plasma. The 10 atm gas puff source produces an atomic density around 10^{19} cm^{-3} in the reservoir which is at least 3 orders of magnitude lower than solid densities; at the jet orifice where the plasma is produced maximum atom densities are probably lower. The x-ray pinhole images of the plasmas produced with this source (Figure 13) show that the laser generates an extended column of plasma with a length of approximately 1 mm and cross-sectional diameter of 100 - 300 μm. This column extended some distance into the jet orifice where it was not visible.

In Figure 14 we compare pulses produced by the gas puff irradiated with both wavelengths as well as a pulse produced with a cryogenic Xe target irradiated with 1.053 μm light. In the gas puff x-ray emission is strong only near the beginning of the pulse and rapidly diminishes before the end of the laser drive pulse. We interpret this temporal behavior to be caused by rapid penetration of the laser through the underdense gas and beyond, where the laser energy was lost and not converted to x-rays. The fact that the emission signal for the 1.053 μm wavelength during the early stages of the pulse is comparable to the signal observed from a solid target shows that, intially, the gas density was high enough to absorb and convert the laser energy to x-rays efficiently. The subsequent decay is probably caused by expansion of the hot plasma to lower densities within the focal volume of the laser beam, which takes place on a nanosecond time scale. A corollary of this result is that

improved coupling and higher conversion might be expected if the same pulse energy could be delivered in a shorter duration, around 1 ns. However, this option is not yet available with the high average power laser technology used in these experiments. The higher conversion with 1.053 μm reflects the fact that the longer wavelength is more efficiently absorbed at this gas density. This is a consequence of the expected inverse bremsstrahlung absorption process in underdense plasma, for which the absorption coefficient[29] scales as λ^2. Thus, at 0.527 μm the absorption coefficient is a factor of 4 weaker largely accounting for the 6-fold smaller x-ray yield; this situation is also consistent with the smaller amplitude and shorter x-ray pulses produced with 0.527 μm light.

Self-absorption by cold Xe gas anywhere between the x-ray source and the detector (or lithography system) turns out to be a significant effect with this type of gas puff source. Cold Xe has an L-shell absorption edge situated around 18 Å; below this wavelength x-rays are absorbed significantly more than above with an absorption coefficient in proportion to the amount of intervening gas. The spectral modifications due to this effect are clearly demonstrated in Figure 15. X-rays in the 10 - 15 Å band are substantially absorbed by about 300 μm of cold Xe at the densities (around 10^{19} cm^{-3}) produced at the nozzle orifice. Absorption from a higher density gas puff will be proportionately more, unless the column of gas is highly confined or collimated.

V. CONCLUSIONS

The intended operating x-ray wavelength of a proximity lithography system will be determined by a number of considerations which are beyond

the scope of the present study. For most situations x-ray wavelengths within the range from 10 Å through 15 Å may be used. The materials selected in this study embrace this wavelength region comprehensively, as summarized in Figure 16. These results demonstrate a significant degree of flexibility in delivering x-ray energy within a desired wavelength band using a laser-produced plasma.

X-ray conversion from all targets increased with increasing laser pulse energy from small values at low pulse energies (< 5 J). A minimum pulse energy of approximately 5 - 10 J was necessary to approach the yields close to the optimum. Above approximately 10 J the yield versus pulse energy curve begins to saturate. This behavior is consistent with the observed saturation of conversion with laser intensity observed by Chaker *et al.*[14] using 0.5 ns pulses, thus indicating that the 10 ns plasma behaves similarly in this pulse energy range. At optimum conditions, the average intensity illuminating the plasma was approximately 5×10^{12} W/cm^2 for 1.053 μm light, and 10^{13} W/cm^2 for 0.527 μm light. For both wavelengths the source size at optimum conversion was approximately 250 - 300 μm in diameter.

Both cryogenic Xe and the Xe gas puff targets offer the attractive possibility of building a reduced debris source. The Xe spectrum contains two main components, with a longer wavelength portion occupying the 17 - 20 Å. For lithography 75% - 80% of the energy is emitted in a 10 - 14 Å band, while 20 - 25% is emitted in the 17 - 20 Å band. At 0.527 μm the 10 - 14 Å portion of the spectrum is significantly harder than with 1.053 μm. While the Xe gas puff offers potentially the most attractive source of this type, the conversion efficiency we measured with the 10 atm Xe gas puff was rather low, attaining about $3\%/2\pi$ sr at best using 1.053 μm laser light. This level is too low for

current proximity lithography needs. Furthermore, it is also evident that cold gas absorption significantly attenuates x-rays at wavelengths less than 18 Å. These factors indicate that the realization of an effective Xe gas puff source will require further effort aimed at increasing the gas pressure or shortening the laser pulse, as well as mitigating against cold gas absorption effects. Solid Xe provides x-ray yields comparable to or better than other solid targets, at both drive wavelengths investigated. In the format of cryogenic pellets, frozen Xe offers the potential for producing a reduced debris source, with yields comparable to solid target yields, and without the finite density and gas absorption problems that arise with a Xe gas puff.

The best yields were attained with type 302 stainless steel targets, which consist of an alloy containing Cr, Ni and Mn as the main components in addition to Fe. This result indicates the possibility for improving x-ray yields by designing mixtures of elements that emit in the desired wavelength band. The high yields of Xe are produced for a similar reason, namely that the much more complicated electronic structure of the Xe M-shell provides many more emission lines to fill in the spectral band than the simpler L-shell emitters.

The x-ray yields produced with the long pulse laser driver used in these experiments matched yields measured previously with shorter (ns-duration) pulses. The duration of the x-ray pulse matched the duration of the laser pulse indicating that, at least in the 12 - 14 ns range, the long pulse duration does not degrade the conversion efficiency. A frequency-doubled Nd:glass laser driver can be used to produce a source with median wavelength anywhere from 10.5 Å to 15 Å at yields that meet the needs of proximity lithography down to 0.12 μm feature size requirements.

ACKNOWLEDGMENTS

We acknowledge technical support from Jim Wintemute, Jim Cox, Ken Haney and Joe Smith. This work was performed under the auspices of the US Department of Energy by Lawrence Livermore National Laboratory under contract W-7405-ENG-48 and was supported by a contract from the US Department of Defense Advanced Research Projects Agency.

REFERENCES

1. K. M. Gilbert, J. P. Anthes, M. A. Gusinow, M. A. Palmer, R. R. Whitlock and D. J. Nagel, *J. Appl. Phys.*, **51**, 1449-1451 (1980).

2. B. Yaakobi, P. Bourke, Y. Conturie, J. Delettrez, J. M. Forsyth, R. D. Frankel, L. M. Goldman, R. L. McCrory, W. Seka, J. M. Soures, A. J. Burek and R. E. Deslattes, *Opt. Commun.*, **38**, 196-200 (1981).

3. H. Nishimura, F. Matsuoka, M. Yagi, K. Yamada, S. Nakai, G. H. McCall and C. Yamanaka, *Phys. Fluids*, **26**, 1688-1692 (1983).

4. D. L. Matthews, E. M. Campbell, N. M. Ceglio, G. Hermes, R. Kauffman, L. Koppel, R. Lee, K. Manes, V. Rupert, V. W. Slivinsky, R. Turner and F. Ze, *J. Appl. Phys.*, **54**, 4260-4268 (1983).

5. W. C. Mead, E. M. Campbell, K. G. Estabrook, R. E. Turner, W. L. Kruer, P. H. Y. Lee, B. Pruett, V. C. Rupert, K. G. Tirsell, G. L. Stradling, F. Ze, C. E. Max, M. D. Rosen and B. F. Lasinski, *Phys. Fluids*, **26**, 2316-2331 (1983).

6. P. Alaterre, H. Pépin, R. Fabbro and B. Faral, *Phys. Rev.*, **A34**, 4184-4194 (1986).

7. T. Mochizuki, T. Yabe, K. Okada, M. Hamada, N. Ikeda, S. Kiyokawa and C. Yamanaka, *Phys. Rev.*, **A33**, 525-539 (1986).

8. R. Popil, P. D. Gupta, R. Fedosejevs and A. A. Offenberger, *Phys. Rev.*, **A35**, 3874-3882 (1987).

9. K. Eidmann and W. Schwanda, *Laser and Particle Beams*, **9**, 551-562 (1991).

10. J. N. Broughton and R. Fedosejevs, *Appl. Phys. Lett.*, **60**, 1818-1821 (1992).

11. D. J. Nagel, M. C. Peckerar, R. R. Whitlock, J. R. Greig and R. E. Pechacek, *Electron. Lett.*, **14**, 781-782 (1978).

12. B. Yaakobi, H. Kim, J. M. Soures, H. W. Deckman and J. Dunsmuir, *Appl. Phys. Lett.*, **43**, 686-688 (1983).

13. H. Pépin, P. Alaterre, M. Chaker, R. Fabbro, B. Faral, I. Toubhans, D. J. Nagel and M. Peckerar, *J. Vac. Sci. Technol.*, **B5**, 27-32 (1987).

14. M. Chaker, H. Pépin, V. Bareau, B. Lafontaine, I. Toubhans, R. Fabbro and B. Faral, *J. Appl. Phys.*, **63**, 892-899 (1988).

15. G. M. Davis, M. C. Gower, F. O'Neill and I. C. E. Turcu, *Appl. Phys. Lett.*, **53**, 1583-1585 (1988).

16. M. Chaker, B. L. Fontaine, C. Y. Côté, J. C. Kieffer, H. Pépin, M. H. Talon, G. D. Enright and D. M. Villeneuve, *J. Vac. Sci. Technol.*, **B10**, 3239-3242 (1992).

17. M. Chaker, J. F. Pelletier and J. C. Kieffer. in *Materials Aspects of X-ray Lithography* (eds. G. K. Celler and J. R. Maldonado) 151-167 (Materials Research Society, San Francisco, CA, USA, 1993).

18. R. Kodama, T. Mochizuki, K. A. Tanaka and C. Yamanaka, *Appl. Phys. Lett.*, **50**, 720-722 (1987).

19. C. B. Dane, L. E. Zapata, W. A. Neuman, M. A. Norton and L. A. Hackel, *IEEE J. Quant. Electron.*, **31**, 148-163 (1995).

20. C. B. Dane, W. A. Neuman and L. A. Hackel, *Opt. Lett.* , **17**, 1271-1273 (1992).

21. H. Fiedorowicz, A. Bartnik, Z. Patron and P. Parys, *Appl. Phys. Lett.* , **62**, 1-3 (1993).

22. Princeton Instruments, Inc., 3660 Quakerbridge Rd., Trenton NJ 08619 USA

23. B. L. Henke, P. Lee, T. J. Tanaka, R. L. Shimabukuro and B. K. Fujikawa, *At. Data Nucl. Data Tables* , **27**, 1-144 (1982).

24. D. R. Kania, L. Pan, H. Korblum, P. Bell, O. L. Landen and P. Pianetta, *Rev. Sci. Instrum.* , **61**, 2765-2767 (1990).

25. D. R. Kania, H. Kornblum, B. A. Hammel, J. Seely, C. Brown, U. Feldman, G. Glendinning, P. Young, E. Hsieh, M. Hennesian, L. DaSilva, B. J. MacGowan, D. S. Montgomery, C. A. Back, R. Doyas, J. Edwards and R. W. Lee, *Phys. Rev.* , **A46**, 7853-7868 (1992).

26. D. R. Kania, L. S. Pan, P. Bell, O. L. Landen, H. Kornblum, P. Pianetta and M. D. Perry, *J. Appl. Phys.* , **68**, 124-130 (1990).

27. Lebow Company, 5960 Mandarin Ave., Goleta, CA 93117 USA

28. J. F. Wyart, C. Bauche-Arnoult, E. Luc-Koenig and TFR Group, *Physica Scripta* , **32**, 103-106 (1985).

29. T. W. Johnston and J. M. Dawson, *Phys. Fluids* , **16**, 722 (1973).

FIGURE CAPTIONS

Figure 1. Experimental arrangement employed for solid target x-ray yield measurements.

Figure 2. Experimental arrangement employed for gas puff x-ray yield measurements.

Figure 3. Sample oscilloscope traces of the laser pulse measured with a photodiode and an x-ray pulse measured with a PCD detector. Vertical scales and temporal offsets for both pulses are arbitrary, and were adjusted for purposes of comparison.

Figure 4. Filter transmission curves for the four types of filters used with the PCD detectors. These were: 10.6 μm thick Al (solid curve); 2.0 μm thick Zn on 1000 Å parylene substrate (long dashed curve); 1.0 μm thick Co (dash - dot curve); and, aluminized mylar consisting of 5000 Å Al on a 1.5 μm thick mylar film (dotted curve). A double layer of the aluminized mylar material was also used as a light shield for the KAP crystal spectrograph.

Figure 5. Variation of x-ray yield with focusing lens position for 1.053 μm laser light; this procedure was used to optimize the yield for a given target type. The origin of the lens position scale is arbitrary.

Figure 6. Variation of x-ray emitting plasma volume with focusing lens postion for 1.053 μm laser light irradiating a solid Fe target. The origin of the lens position scale is arbitrary. Displayed in (a) is a sequence of pinhole photographs of the plasma x-ray emission taken at various lens positions

(indicated on the individual frames). In (b) is the variation of plasma size with lens position measured from the pinhole photographs. Also shown for comparison is the beam size assuming a geometric f/13 focal cone with best focus assumed to occur at the lens position producing the smallest plasma volume.

Figure 7. Similar to Figure 6, except with 0.527 μm laser light irradiating a type 302 stainless steel solid target.

Figure 8. Angular distribution of x-ray emission relative to target normal measured for 14 Å emitters (Fe or type 302 stainless steel) at both drive wavelengths.

Figure 9. Optimized x-ray conversion fractions measured for all solid targets and both drive wavelengths.

Figure 10. X-ray spectra measured for all solid targets using 1.053 μm laser light. Spectral intensity is displayed on the arbitrary left hand scale; the wavelength integrated x-ray yield for each material can be measured against the right hand scale. Conversion fraction indicates the ratio of x-ray energy divided by incident laser energy. Target materials are (a) type 302 stainless steel; (b) Fe; (c) solid Xe; (d) Cu; (e) brass; and, (f) Zn.

Figure 11. Same as for Figure 10, except using 0.527 μm laser light.

Figure 12. Pulse energy dependence of x-ray yield for two target materials and a both drive wavelengths. Target materials are: (a) type 302 stainless steel; and, (b) Cu.

Figure 13. X-ray emission column observed with the Xe gas puff target irradiated with (a) 1.053 μm laser light; and, (b) 0.527 μm laser light.

Figure 14. X-ray pulses emitted from a Xe gas puff target and recorded on a PCD detector. Emission pulses from the gas puff target irradiated with 1.053 μm laser light and 0.527 μm laser light are compared with the emission pulse observed from a solid Xe target irradiated with 1.053 μm laser light.

Figure 15. X-ray spectra emitted from a Xe gas puff target with varying amounts of cold Xe gas situated between the plasma column and the spectrograph. Cold Xe gas thicknesses were approximately (a) 600 μm; (b) 300 μm; and, (c) 0 μm.

Figure 16. Emission wavelengths determined from the spectra measured for all the solid elements at both laser drive wavelengths. The bar end points indicate wavelengths spanning 10% to 90% of the wavelength-integrated emission (i.e. containing 80% of the emission). The points within the bars indicate the median emission wavelengths (50% point on the integral curve) for each material. *In the special case of solid Xe, this evaluation was restricted to wavelengths less than 16 Å, which eliminates the long wavelength emission component (≈ 18 Å) from the weighting process.

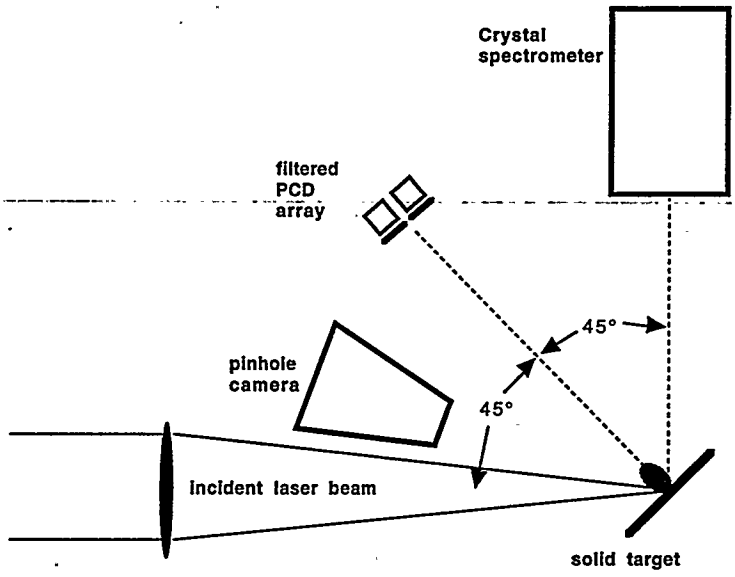
Crystal
spectrometer
filtered
PCD
array
45°
pinhole
camera
45°
incident laser beam
solid target

Figure 1

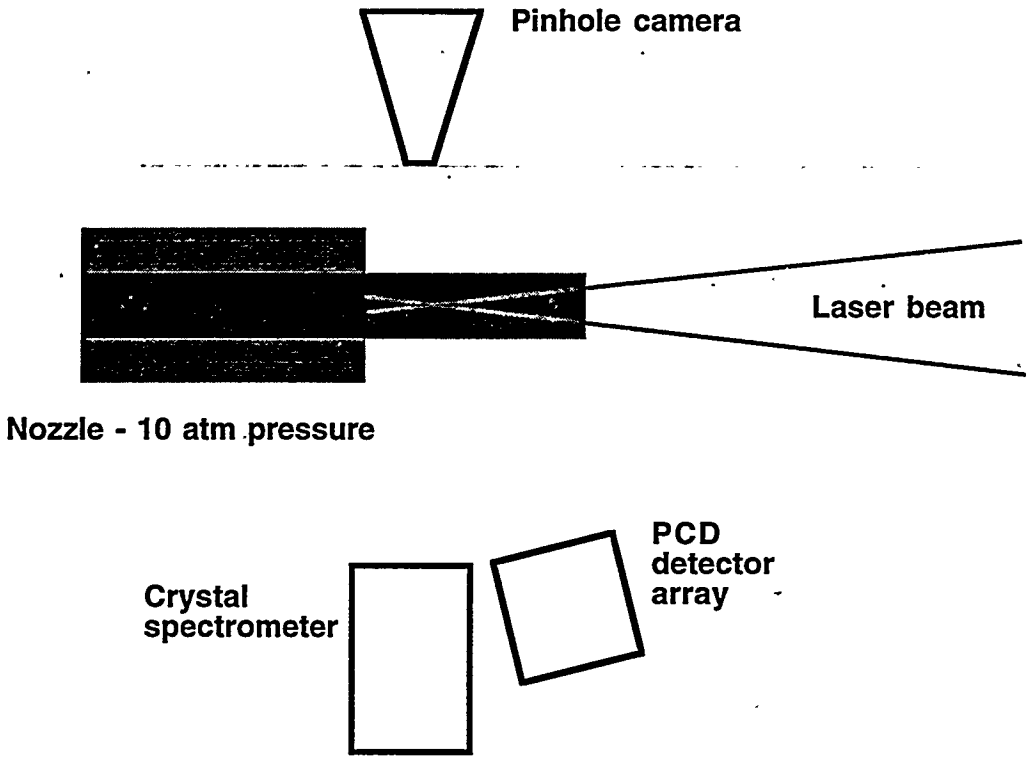
Pinhole camera
Laser beam
Nozzle - 10 atm pressure
PCD
detector
array
Crystal
spectrometer

Figure 2

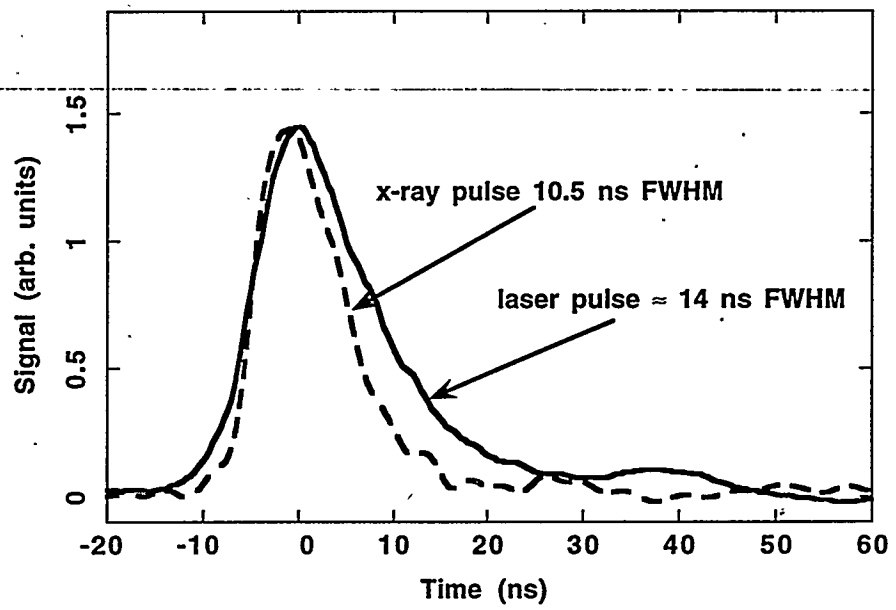
Signal (arb. units)
0
0.5
1
1.5
-20
-10
0
10
20
30
40
50
60
Time (ns)
x-ray pulse 10.5 ns FWHM
laser pulse ≈ 14 ns FWHM

Figure 3

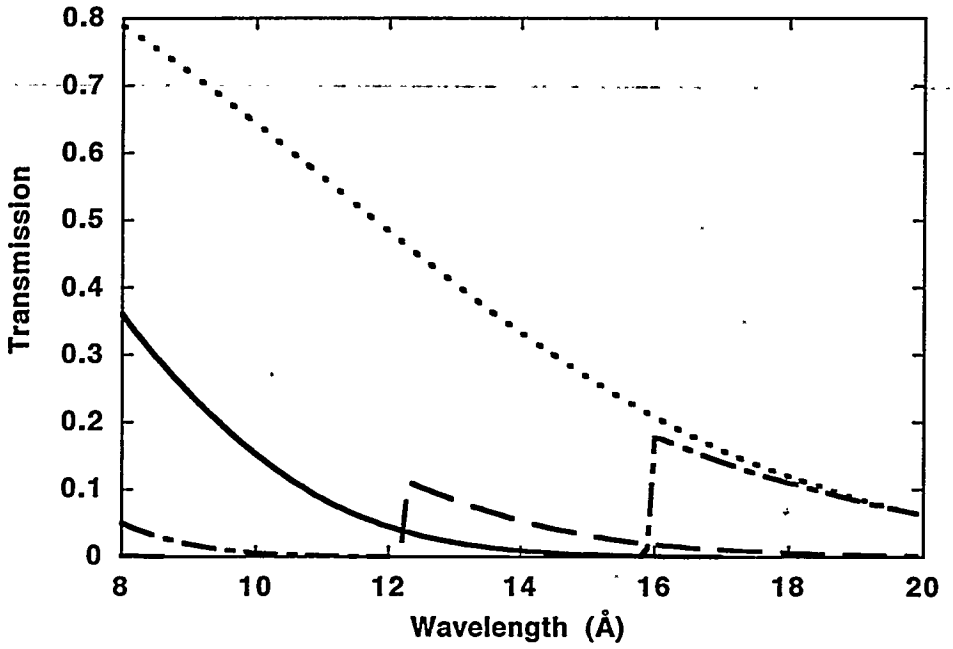
Transmission
0.8
0.7
0.6
0.5
0.4
0.3
0.2
0.1
0
8
10
12
14
16
18
20
Wavelength (Å)

Figure 4

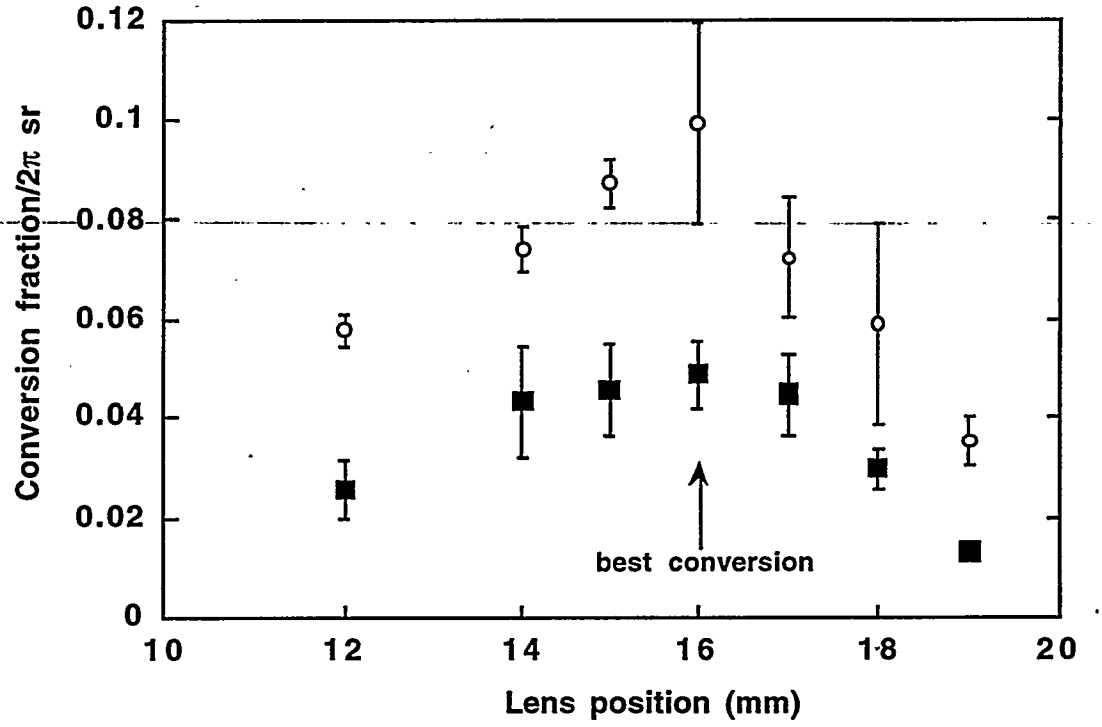
0.12
0.1
0.08
0.06
0.04
0.02
0
Conversion fraction/2π sr
best conversion
10
12
14
16
18
20
Lens position (mm)

Figure 5

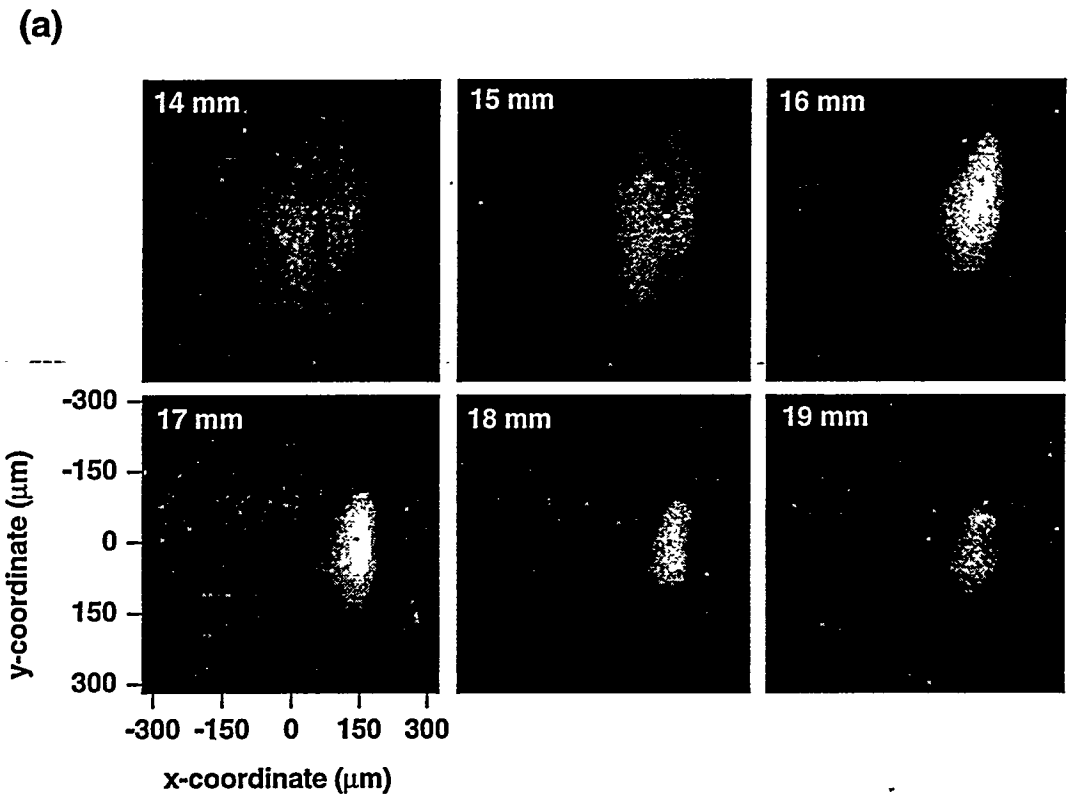
(a)
14 mm
15 mm
16 mm
17 mm
18 mm
19 mm
-300
-150
0
150
300
y-coordinate (μm)
-300 -150 0 150 300
x-coordinate (μm)

Figure 6 (a)

(b)

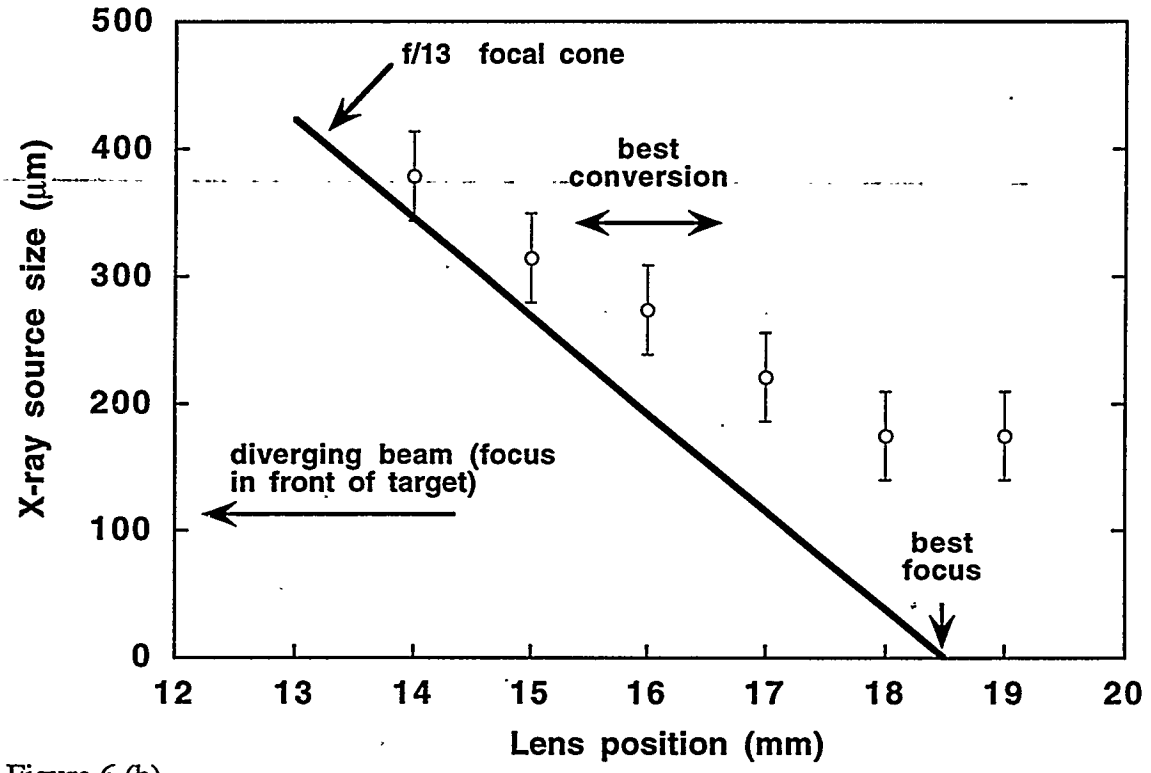
500
400
300
200
100
0
X-ray source size (μm)
f/13 focal cone
best
conversion
diverging beam (focus
in front of target)
best
focus
12
13
14
15
16
17
18
19
20
Lens position (mm)

Figure 6 (b)

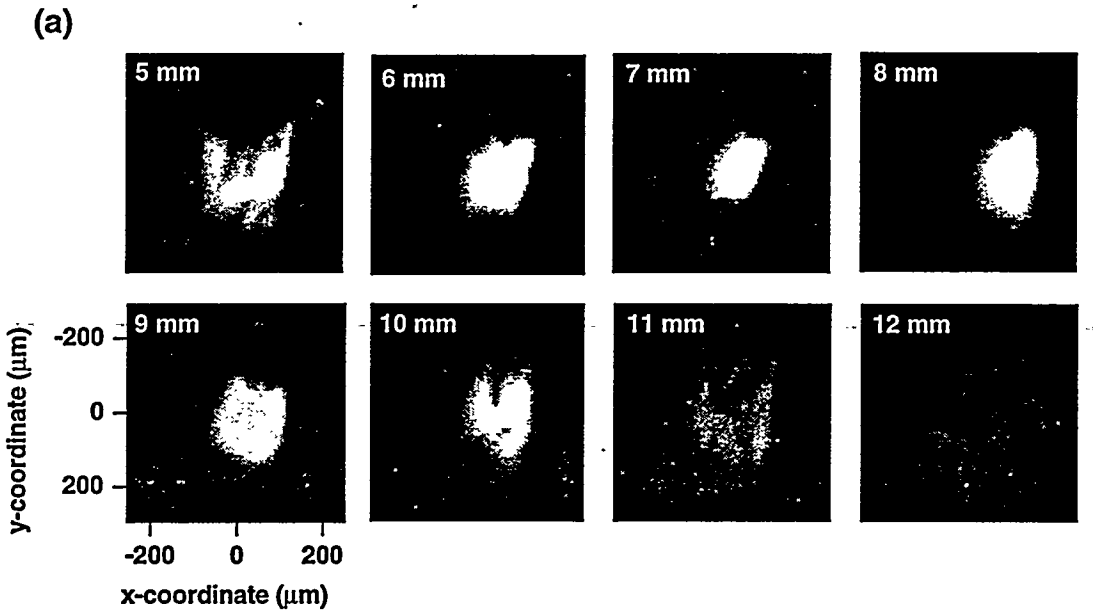
(a)
5 mm
6 mm
7 mm
8 mm
9 mm
10 mm
11 mm
12 mm
y-coordinate (μm)
-200
0
200
-200
0
200
x-coordinate (μm)

Figure 7 (a)

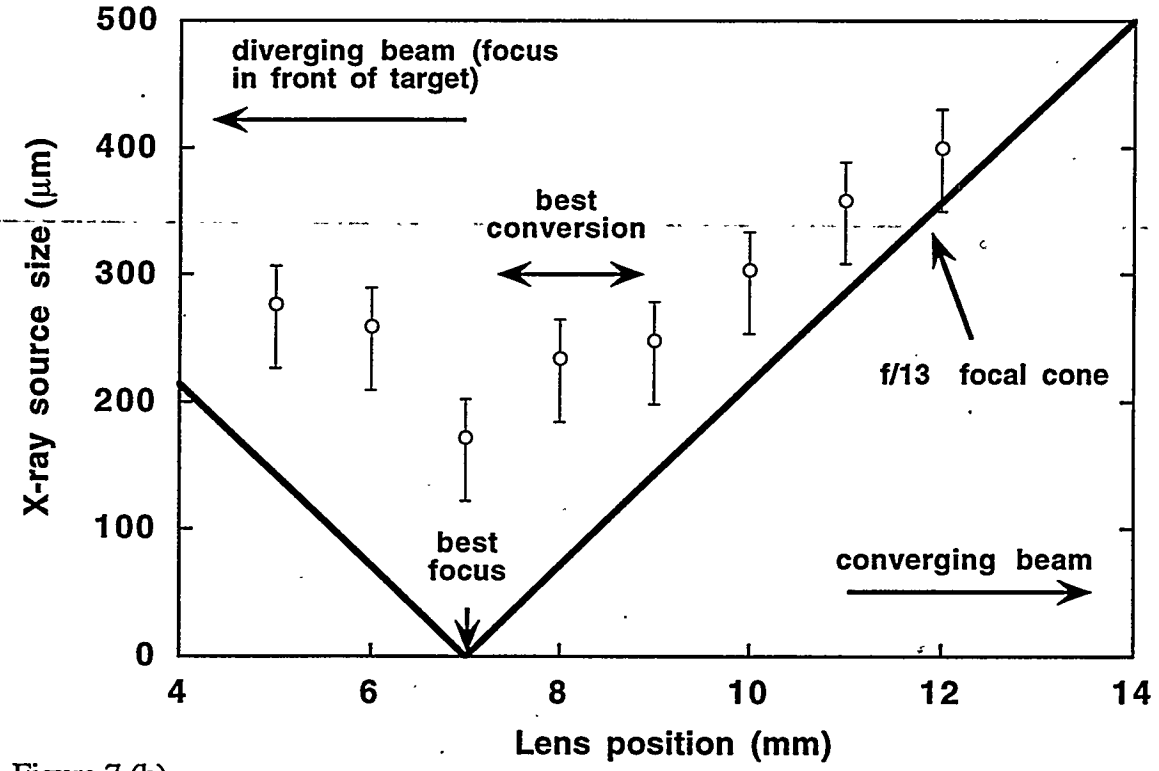
500
400
300
200
100
0
X-ray source size (μm)
diverging beam (focus in front of target)
best conversion
best focus
converging beam
f/13 focal cone
4
6
8
10
12
14
Lens position (mm)

Figure 7 (b)

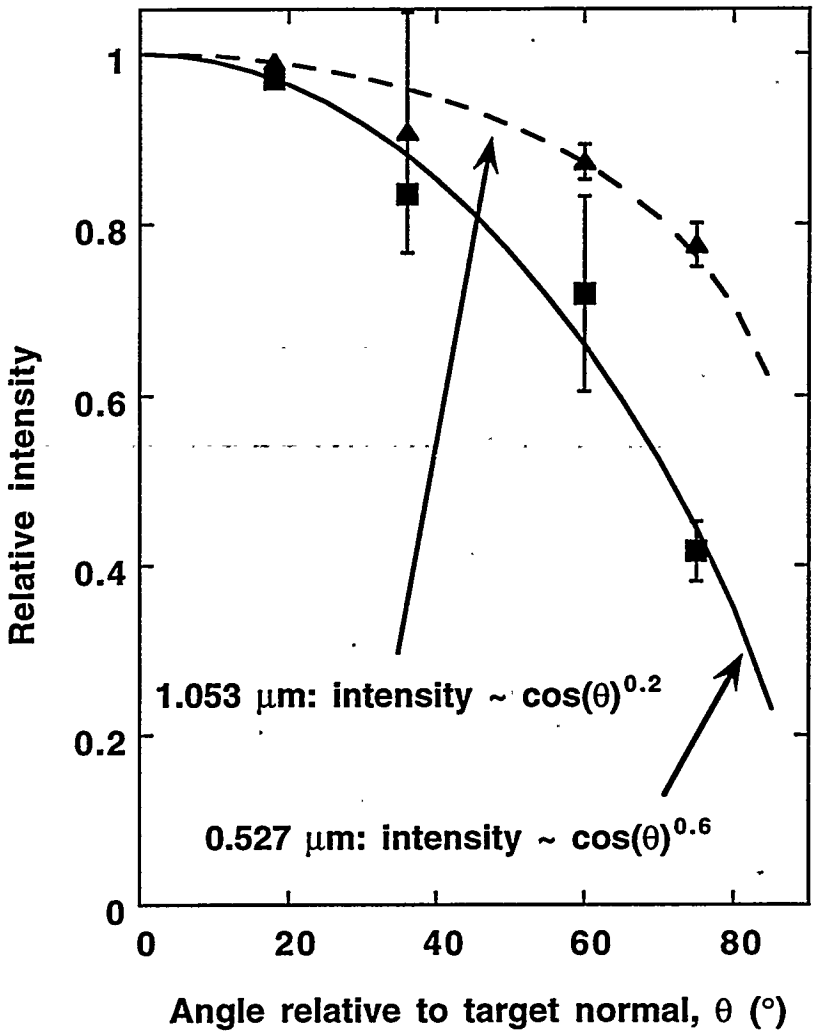
Relative intensity
1
0.8
0.6
0.4
0.2
0
0
20
40
60
80
1.053 μm: intensity ~ cos(θ)^0.2
0.527 μm: intensity ~ cos(θ)^0.6
Angle relative to target normal, θ (°)

Figure 8

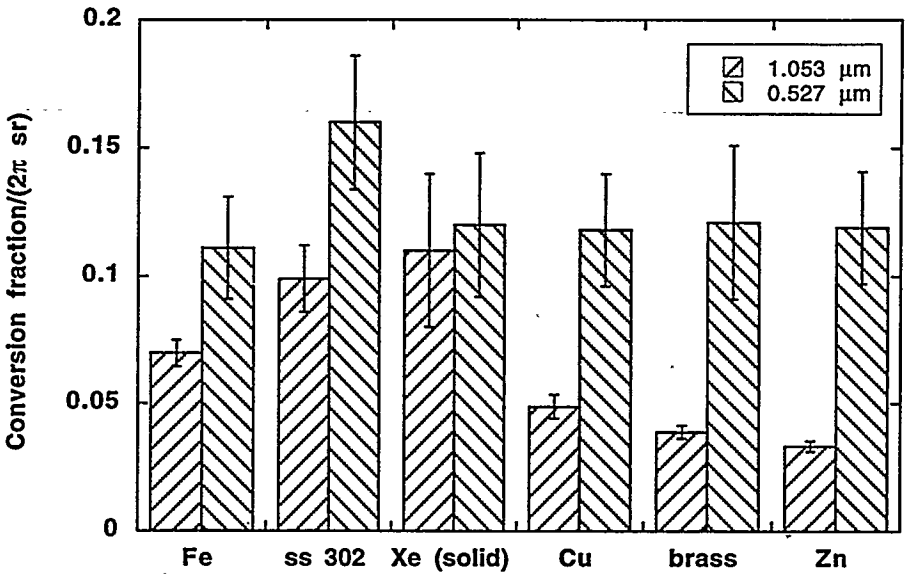
0.2
0.15
0.1
0.05
0
Conversion fraction/(2π sr)
1.053 μm
0.527 μm
Fe
ss 302
Xe (solid)
Cu
brass
Zn

Figure 9

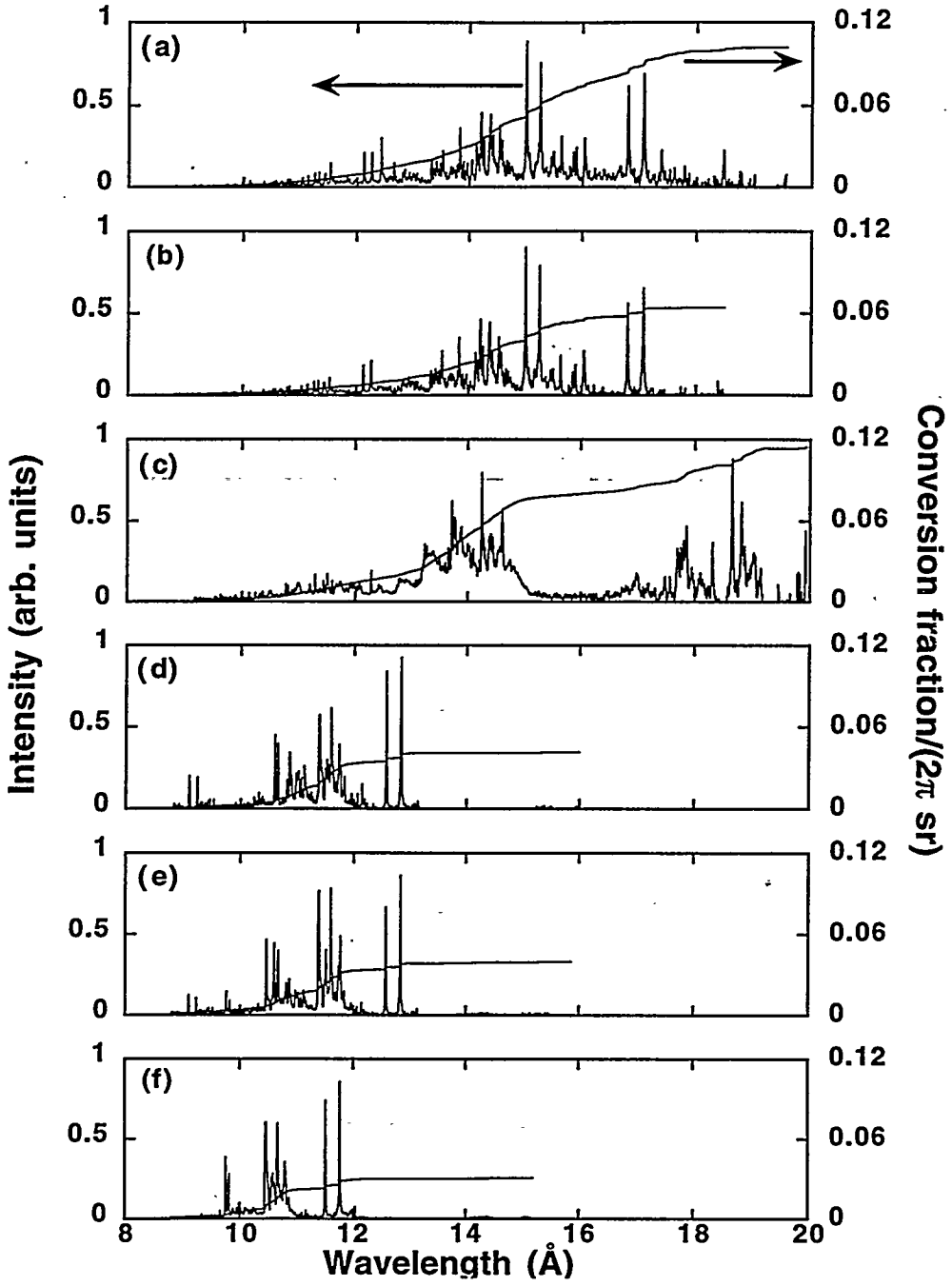
(a)
(b)
(c)
(d)
(e)
(f)
Intensity (arb. units)
Conversion fraction/(2π sr)
Wavelength (Å)
1
0.5
0
0.12
0.06
8
10
12
14
16
18
20

Figure 10

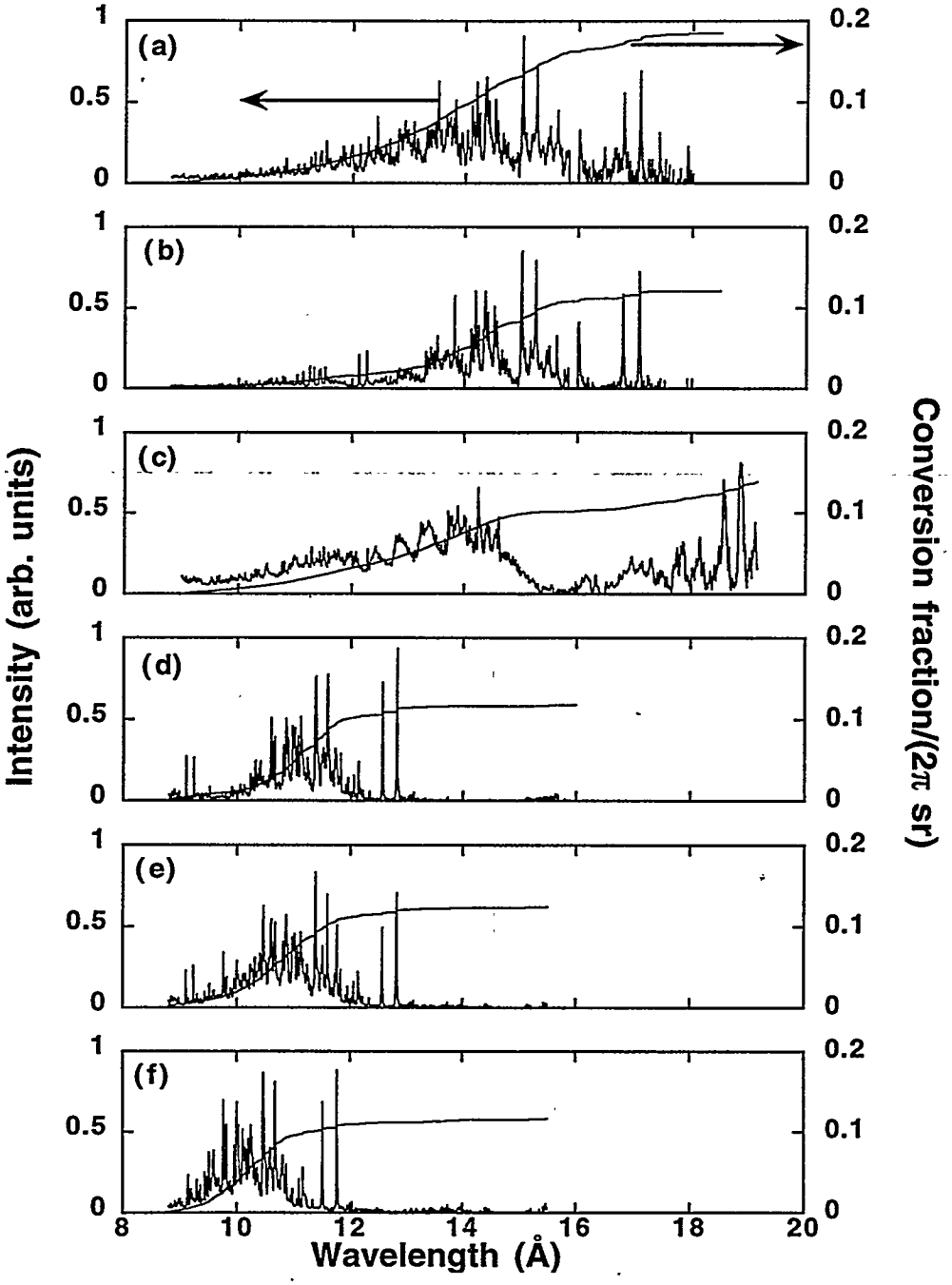
(a)
(b)
(c)
(d)
(e)
(f)
Intensity (arb. units)
Conversion fraction/(2π sr)
Wavelength (Å)
0
0.5
1
0.1
0.2
8
10
12
14
16
18
20

Figure 11

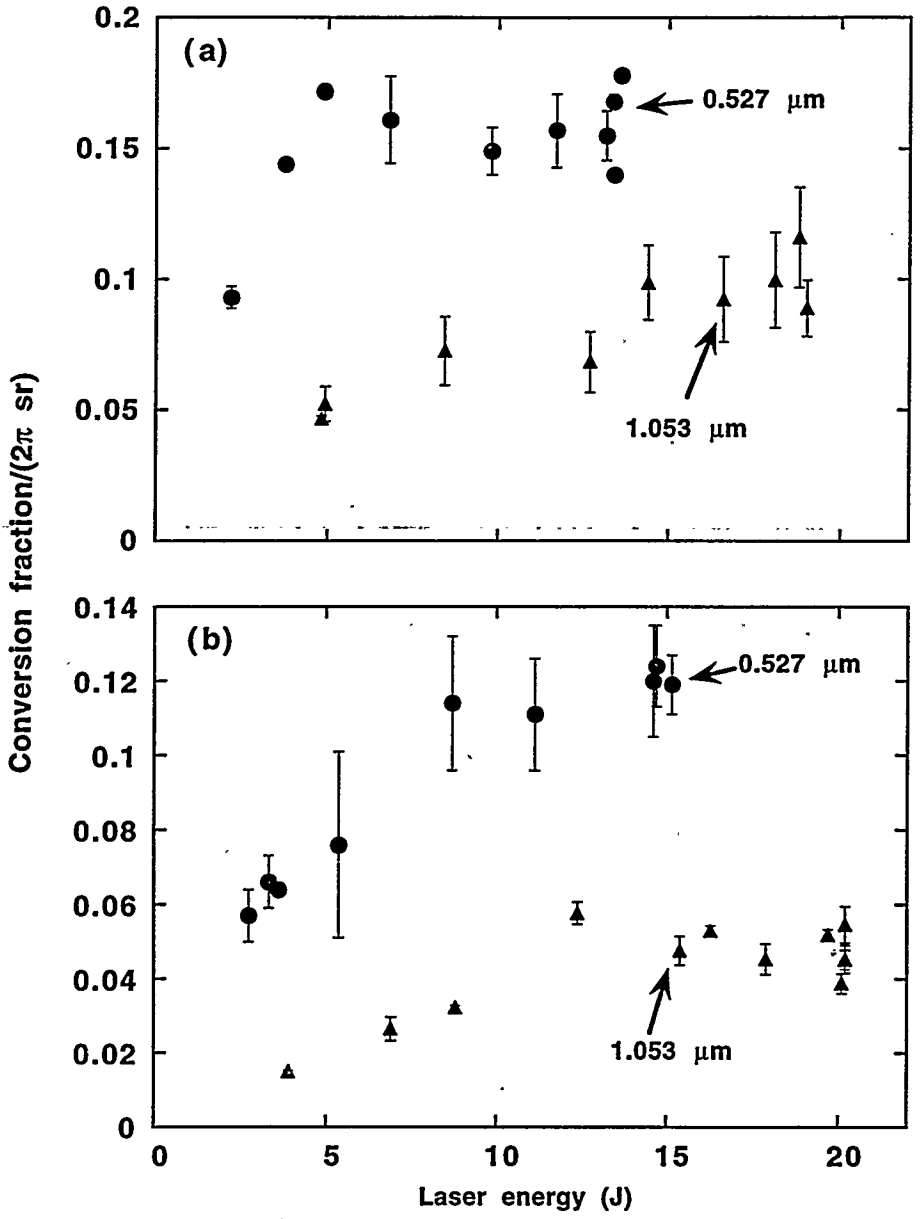
(a)
0.527 μm
1.053 μm
(b)
0.527 μm
1.053 μm
Conversion fraction/(2π sr)
Laser energy (J)
0.2
0.15
0.1
0.05
0
0.14
0.12
0.1
0.08
0.06
0.04
0.02
0
0
5
10
15
20

Figure 12

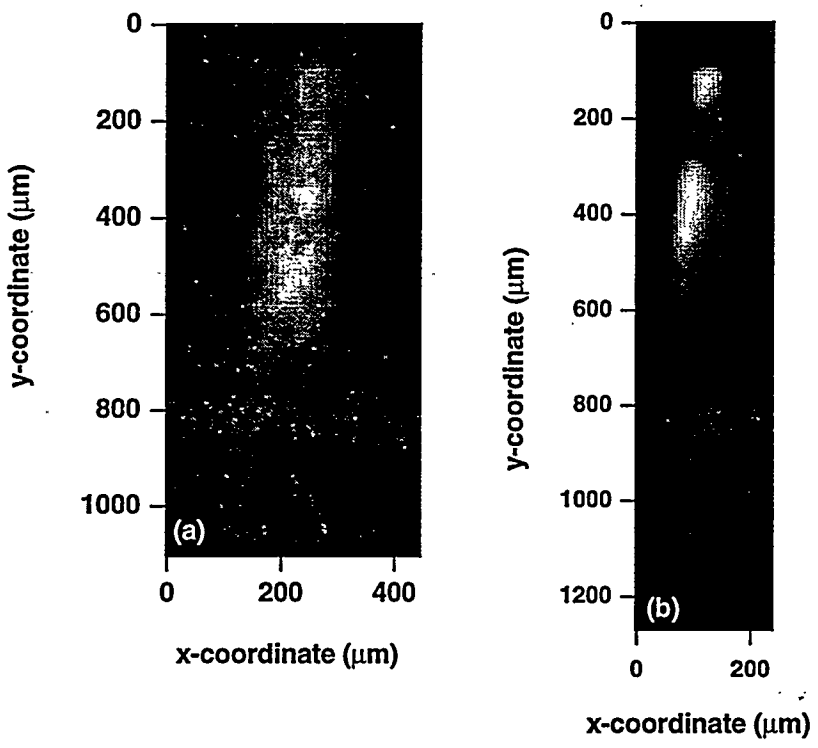
0
200
400
600
800
1000
y-coordinate (μm)
(a)
0
200
400
x-coordinate (μm)
0
200
400
600
800
1000
1200
y-coordinate (μm)
(b)
0
200
x-coordinate (μm)

Figure 13

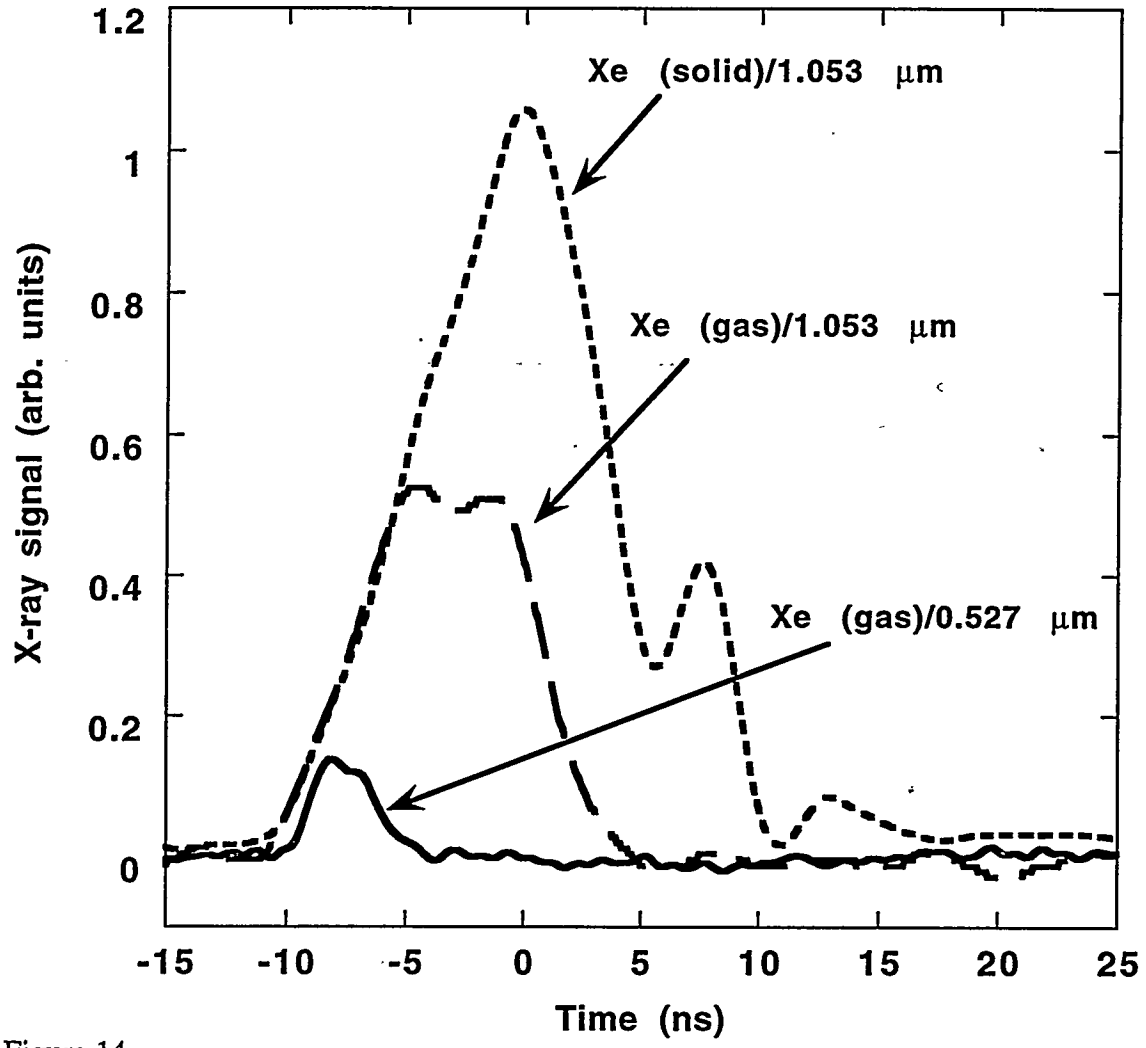
Xe (solid)/1.053 μm
Xe (gas)/1.053 μm
Xe (gas)/0.527 μm
X-ray signal (arb. units)
Time (ns)
1.2
1
0.8
0.6
0.4
0.2
0
-15
-10
-5
0
5
10
15
20
25

Figure 14

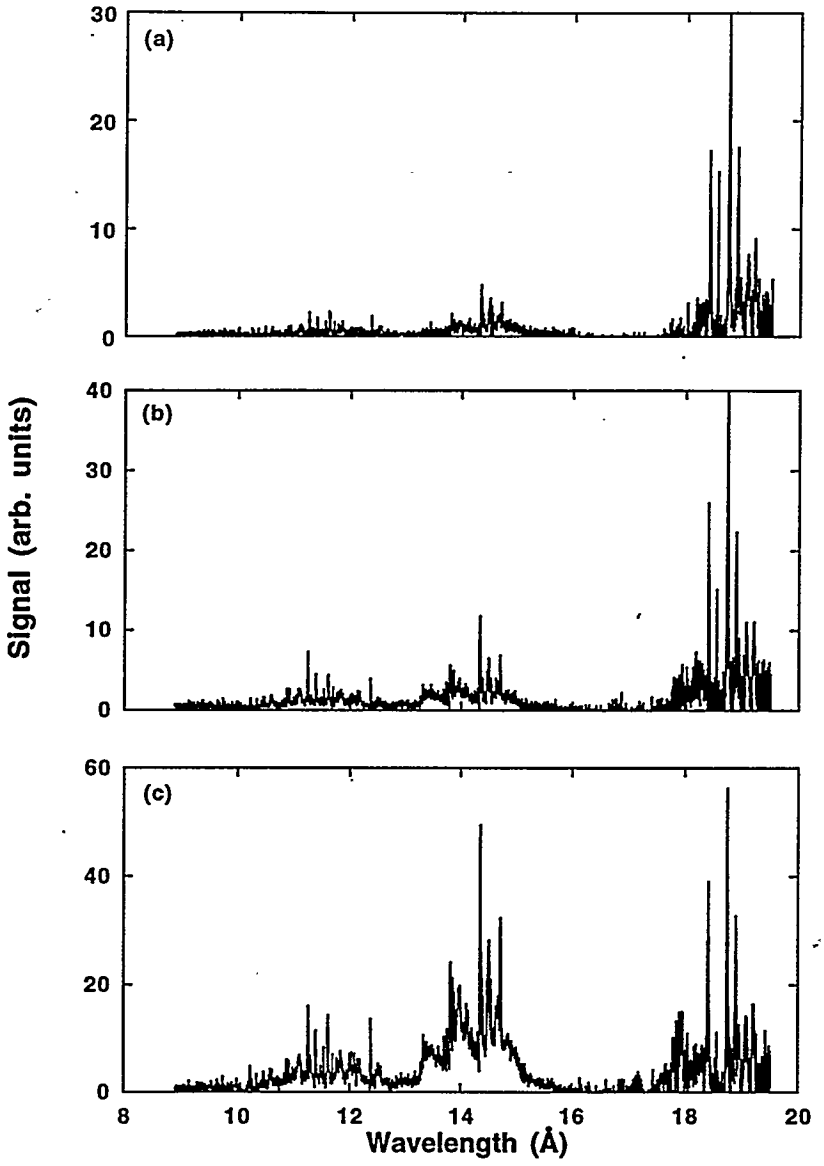
(a)
(b)
(c)
Signal (arb. units)
Wavelength (Å)
0
10
20
30
40
60
8
10
12
14
16
18
20

Figure 15

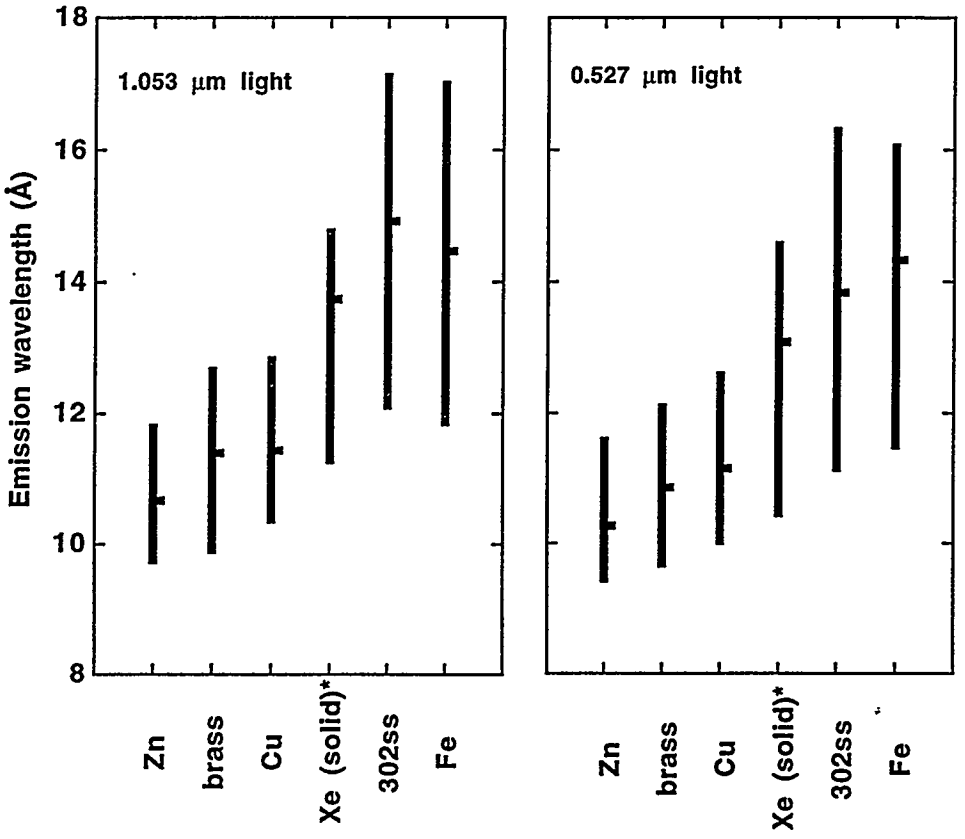
1.053 μm light
0.527 μm light
Emission wavelength (Å)
18
16
14
12
10
8
Zn
brass
Cu
Xe (solid)*
302ss
Fe

Figure 16

Technical Information Department • Lawrence Livermore National Laboratory
University of California • Livermore, California 94551